

See discussions, stats, and author profiles for this publication at: <https://www.researchgate.net/publication/231629095>

Semiclassical Dynamics in the Coherent Control of Nonadiabatic ICN Photodissociation†

ARTICLE *in* THE JOURNAL OF PHYSICAL CHEMISTRY A · FEBRUARY 2001

Impact Factor: 2.69 · DOI: 10.1021/jp0035939

CITATIONS

19

READS

5

2 AUTHORS, INCLUDING:



Paul Brumer

University of Toronto

323 PUBLICATIONS 8,104 CITATIONS

SEE PROFILE

Semiclassical Dynamics in the Coherent Control of Nonadiabatic ICN Photodissociation[†]

Victor S. Batista* and Paul Brumer

Chemical Physics Theory Group, Department of Chemistry, and Photonics Research Ontario, University of Toronto, Toronto, Ontario M5S 3H6, Canada

Received: October 2, 2000

The utility of a semiclassical initial value representation (SC-IVR) to simulate coherent control is explored. Specifically, bichromatic control of the state specific ICN photodissociation in the \tilde{A} continuum is investigated both quantum mechanically and semiclassically, and the ability of the SC-IVR method to reproduce *phases* of transition matrix element products is examined. Control over the $I(^2P_{1/2})/I(^2P_{3/2})$ product ratio is considerable and the resultant semiclassical photofragmentation ratios are in good agreement with full quantum dynamics calculations.

I. Introduction

Understanding, manipulating, and utilizing laser-induced quantum interference effects in chemical reaction dynamics is a central problem in the development of the new optical technology to control atomic and molecular processes. These quantum mechanical effects require detailed investigation using new computational techniques for modeling excited state chemical dynamics. Indeed, quantum mechanics simulations have already proven useful in understanding and developing coherent control techniques.¹ However, these rigorous computational methods are currently limited to systems with only a few degrees of freedom, since they usually require computational effort and storage space that scales exponentially with the number of coupled degrees of freedom. Future computations of larger systems must, in the foreseeable future, rely on developments in semiclassical dynamics techniques.

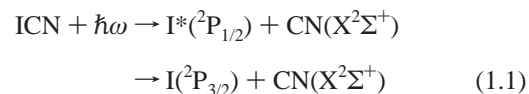
In this paper we examine the utility of semiclassical initial value representation SC-IVR techniques for coherent optical control simulations, and we investigate coherent control of nonadiabatic ICN photodissociation in the \tilde{A} continuum. Specifically, we consider control of the I/I^* ratio in ICN photodissociation using the bichromatic coherent control scenario.^{2,3} In this scenario, two lasers are used to photodissociate ICN, prepared in a superposition of coherent states. Control can be achieved by varying the relative phases and intensities of the two photodissociation lasers, or by varying the expansion coefficients in the superposition state. This particular coherent control scenario has yet to be demonstrated experimentally but has been investigated theoretically, using quantum mechanical simulations as applied to ICH_3 photodissociation dynamics, demonstrating a broad range of control over the possible photofragmentation channels.^{2,3}

Of particular interest in this paper is the SC-IVR approach, which is a generalization of classical molecular dynamics simulation methods. This approach combines the quantum superposition of probability amplitudes with real-valued classical trajectories in the computation of the quantum mechanical propagator.^{4–17} These methods aim to provide a tractable alternative to exact quantum mechanical computations¹⁸ as well as an intuitive understanding of complex quantum dynamics

associated with chemical reactions. In this paper we implement a SC-IVR approach that is able to describe electronically nonadiabatic processes through the quantization of the classical electron–nuclear model Hamiltonian of Meyer and Miller.¹⁹ This SC method has been successfully applied to the three 1-dimensional model problems suggested by Tully for testing nonadiabatic dynamics,²⁰ and to the spin-boson model for dissipative systems.^{21,22} However, the only applications to date for a real molecular system have been the studies of ultrafast photodissociation dynamics of ozone,⁵ and the nonadiabatic photodissociation dynamics of ICN in the \tilde{A} continuum.²³ The latter computations demonstrated the capabilities of the SC-IVR for simulating both the absorption band, and the rotational distributions of CN photofragments. There remains, however, the nontrivial question as to whether this method can also be successfully implemented to simulate coherent control, which requires quantum phases as well as amplitudes.

In this paper we show that such semiclassical approach can indeed be effectively implemented to describe the complex quantum interference terms required in coherent control of ICN photodissociation dynamics. Specifically, we evaluate the cumulative ICN state specific photofragmentation amplitudes using the Herman–Kluk SC-IVR methodology, together with stationary phase MC methods (see refs 5 and 23). For the sake of presenting a rigorous comparison between semiclassical and full quantum mechanical results, we solve first the scattering problem at the complete state-to-state level, and then compute the cumulative transition amplitudes by summing over final states. As a byproduct we also produce the cross sections for ICN photodissociation into various product channels with excitation from a variety of initial ICN states.

The ICN \tilde{A} continuum is a broad absorption band in the 200–300 nm range.²⁴ Photolysis at approximately 266 nm induces predominately $^3\Pi_{0+} \leftarrow X$ parallel transitions, and produces two peaks in the translational photofragment spectra. These peaks are assigned to two photodissociation pathways, indicated below



that produce either iodine atoms in the $I^*(^2P_{1/2})$ spin–orbit state, through adiabatic photodissociation, or iodine atoms in the

[†] Part of the special issue “William H. Miller Festschrift”.

$I(^2P_{3/2})$ spin-orbit state, through nonadiabatic dynamics at the conical intersection between electronic excited states $^3\Pi_{0+}$ and $^1\Pi_1$, respectively. Here $\hbar\omega$ is the photoexcitation energy, and the CN radicals are produced in the ground electronic state CN- ($X^2\Sigma^+$). Little vibrational excitation is found in the CN fragment ($>98\%$ in $v=0$), but the rotational distribution of CN involves highly excited states and exhibits a bimodal structure.²⁵ Experiments have shown that the CN fragment is formed with rotational distributions that peak at low quantum numbers when dissociation of the molecule produces excited state iodine atoms $I^*(^2P_{1/2})$. The channel forming ground state iodine $I(^2P_{3/2})$, however, produces CN fragments that are rotationally hot. Experiments have also shown that the I/I^* branching ratio in the CN rotational distribution is not very sensitive to the initial temperature of the parent molecule but can be strongly controlled in terms of the photoexcitation wavelength, with I^* production accounting for approximately 62% of the total product at 266 nm, but much less at both lower and higher photoexcitation energies.²⁶

In this paper we show that the I/I^* branching ratio can also be controlled over a broad range of values, simply by changing the relative phases of two laser pulses that photoexcite an initial superposition state to the same final energy state in the \tilde{A} continuum. Considering the longstanding interest in ICN photodissociation, we anticipate considerable experimental interest in examining this control scenario.

The paper is organized as follows. In section II we first outline the CC technique based on bichromatic excitation of a superposition state, and the SC-IVR methods implemented in our simulations to calculate the degree of yield control in terms of state-to-state specific transition matrix elements. Section III then summarizes our semiclassical results, and compares them with full quantum dynamics simulations. Section IV summarizes and concludes.

II. Methods

A. Bichromatic Coherent Control. We consider bichromatic coherent control in a model of ICN photodissociation.^{2,3} In accord with this scenario, the system is prepared in an initial superposition state

$$|\Psi_0(j,k)\rangle = |\Phi_g\rangle(c_j|\chi_0(j)\rangle + c_k|\chi_0(k)\rangle) \quad (2.1)$$

where $|\Phi_g\rangle$ is the ICN ground electronic state wave function. Here $|\chi_0(j)\rangle$ is the nuclear eigenstate of energy E_j associated with excitation in the j -th vibrational state of the Jacobi coordinate R , which represents the distance between the iodine atom and the CN center of mass. The system is subsequently photoexcited with two CW lasers with frequencies ω_j and ω_k , where $\omega_j = E - E_j$, and E represents the final energy of the system after photoexcitation to the \tilde{A} continuum. That is, we excite the system with the electric field $\epsilon(t)$

$$\bar{\epsilon}(t) = \bar{\epsilon}_j e^{-i(\omega_j t + \theta_j)} + \bar{\epsilon}_k e^{-i(\omega_k t + \theta_k)} + \text{c.c.} \quad (2.2)$$

where $\bar{\epsilon}_j$ and $\bar{\epsilon}_k$ are time independent vectors of length $|\bar{\epsilon}_j|$ and $|\bar{\epsilon}_k|$. θ_j and θ_k are the phases of the two pulses. As a consequence, both $|\chi_0(j)\rangle$ and $|\chi_0(k)\rangle$ are raised by the laser field with frequencies ω_j and ω_k , to states with energy E in the continuum, denoted $|E, \xi, J\rangle$. Here J is the CN angular momentum and $\xi = (I_{1/2} \text{ or } I_{3/2})$, denotes the state of the iodine product. The CN vibration is ignored since experiments show little CN vibrational excitation after photodissociation. These two photoexcitation routes interfere with one another.

Assuming that the field is sufficiently weak to allow the use of first-order perturbation theory, the relative product ratio $R(\xi, \xi', E)$, of producing product in arrangement channel ξ to that in arrangement ξ' , at energy E , is given by

$$R(\xi, \xi', E) = \{|\mu_{jj}(\xi, E)| + x^2 |\mu_{kk}(\xi, E)| + 2x \cos(\theta_j - \theta_k + \Phi_{jk}(\xi, E)) |\mu_{jk}(\xi, E)|\} / \{|\mu_{jj}(\xi', E)| + x^2 |\mu_{kk}(\xi', E)| + 2x \cos(\theta_j - \theta_k + \Phi_{jk}(\xi', E)) |\mu_{jk}(\xi', E)|\} \quad (2.3)$$

Here x is the ratio of controllable parameters $x = |(c_k/\bar{\epsilon}_k)|/(c_j/\bar{\epsilon}_j)|$, and $\Phi_{jk}(\xi, E)$ is the phase of the cumulative transition matrix element $\mu_{jk}(\xi, E)$, where

$$\mu_{j,k}(\xi, E) = |\mu_{jk}(\xi, E)| e^{i\Phi_{jk}(\xi, E)} = \sum_{J=0}^{\infty} \langle \chi_0(k) | \mu_\epsilon | E, \xi, J^- \rangle \langle E, \xi, J^- | \mu_\epsilon | \chi_0(j) \rangle \quad (2.4)$$

with μ_ϵ being the dipole operator along the direction of the field. Note that the off-diagonal μ_{jk} manifest the interference between components of the continuum wave function which are excited by independent coherent excitation pathways. The matrix element $\langle E, \xi, J^- | \mu_\epsilon | \chi_0(j) \rangle$ in eq 2.4, is the state-to-state specific transition matrix element associated with the initial vibrational state $|\chi_0(j)\rangle$, and the final photodissociation channel corresponding to electronic state ξ , CN rotational state J , energy E , and incoming boundary conditions.

Equations 2.3 and 2.4 show that the relative product yield $R(I_{1/2}:I_{3/2}, E)$ of product in $I_{1/2}$ to product in $I_{3/2}$ can be computed in terms of the state-to-state specific transition matrix elements $\langle E, \xi, J^- | \mu_\epsilon | \chi_0(j) \rangle$, and can be experimentally controlled by changing either the initial superposition state, or the relative phase and amplitude of the CW photoexcitation lasers.

The state-to-state specific transition matrix elements are obtained in the time dependent picture by evolving each wave packet component $|\chi_0(j)\rangle$ in the initial superposition times the dipole function, to obtain $|\chi_t(j)\rangle$ as determined by the nonadiabatic excited state dynamics at time t . We then compute the desired matrix element as

$$\langle E, \xi, J^- | \mu_\epsilon | \chi_0(j) \rangle \equiv \lim_{t \rightarrow \infty} \langle K(E), J, \xi | \chi_t(j) \rangle e^{iEt/\hbar} \quad (2.5)$$

where $\langle K, J, \xi | \chi_t(j) \rangle$ is the asymptotic nuclear wave packet, in the $K - J$ representation, associated with the final electronic state ξ . Note that the integral associated with the rhs of eq 2.5 should include the appropriate Jacobian factors. Here K is the nuclear momentum conjugate to the Jacobi coordinate R , and $K(E)$ is its asymptotic value at final energy E and CN rotational state J , given by the formula

$$K(E) = \left[2M \left(\frac{E - E_0(\xi)}{\hbar^2} - \frac{J(J+1)}{2mr^2} \right) \right]^{1/2} \quad (2.6)$$

where $E_0(\xi)$ is the asymptotic energy of the electronic state potential energy surface associated with photodissociation channel ξ , M is the reduced mass associated with coordinate R , and m is the C-N reduced mass.

To obtain $\langle K, \xi, J | \chi_t(j) \rangle$, we compute the asymptotic wave function $\langle \mathbf{x}, R, \theta | \Psi_t(j) \rangle$ that results from nonadiabatic dynamics propagation, after instantaneous photoexcitation of the $|\Phi_g\rangle|\chi_0(j)\rangle$ state component in the initial superposition to the optically active electronic excited state resonant with the excitation energy. Here \mathbf{x} are the electronic degrees of freedom,

and Θ is the angle between the I to CN distance and the CN axis. Projecting out the corresponding electronic state $|\phi^\xi\rangle$ gives

$$\Psi_i^\xi(R, \theta; j) = \int d\mathbf{x} \langle \phi^\xi | \mathbf{x} \rangle \langle \mathbf{x}, R, \theta | \Psi_i(j) \rangle \quad (2.7)$$

and transforming $\Psi_i^\xi(R, \theta; j)$ to the K - J representation according to

$$\langle K, J, \xi | \chi_i(j) \rangle = A \int_0^\infty dR \int_0^\pi d\Theta Y_{J0}^*(\Theta) \sin \Theta e^{-iKR} \Psi_i^\xi(R, \Theta; j) \quad (2.8)$$

gives the desired $\langle K, J, \xi | \chi_i(j) \rangle$. Here A is a normalization constant, and the spherical harmonic $Y_{J0}(\Theta)$ represents the J -th rotational state of the CN fragment. The computational task for predicting the degree of yield control is therefore reduced to calculating the cumulative transition matrix elements $\mu_{ij}(\xi, E)$, in terms of the asymptotic state components $|\Psi_i(j)\rangle$ obtained according to the SC-IVR methodology described in section IIB.

B. State-Resolved Semiclassical Approach. The semiclassical approach considered in this paper computes $\mu_{ij}(\xi, E)$ from $|\chi_i(j)\rangle$, in accord with eqs 2.4 and 2.5. The $|\chi_i(j)\rangle$ are computed by propagating each state $|\Psi_0(j)\rangle$ in the initial superposition according to the semiclassical methodology outlined in ref 23. Specifically, the Herman–Kluk propagator is used in conjunction with a stationary phase Monte Carlo method to simulate nonadiabatic dynamics using the Miller–Meyer Hamiltonian for the ICN system. This Hamiltonian includes both electronic and nuclear degrees of freedom.

Semiclassical results were found to be converged with 2×10^7 trajectories, using the parallel programming model described in ref 5. However, we have observed that a good qualitative description of coherence control can already be obtained with an ensemble of 2×10^6 trajectories. For comparison purposes, we computed quantum mechanical results using the fast Fourier transform (FFT) method with an extended grid of 512 points in both the R and Θ coordinates, defined in the range of coordinates $|R - 9| \text{ au} < 5 \text{ au}$, and $|\Theta| < 2\pi$ radians.

The initial wave packet components $\Psi_0(\mathbf{x}, R, \theta; j)$, after instantaneous photoexcitation of the system, are defined according to the Meyer–Miller formalism as a product of electronic and nuclear wave functions

$$\Psi_0(\mathbf{x}, R, \theta; j) = \phi^n(\mathbf{x}) \chi_0(j; R, \theta) \quad (2.9)$$

assuming that the transition dipole that couples the ground electronic state g with the optically active electronic excited state n is independent of nuclear coordinates (Condon approximation). We take as $\chi_0(j; R, \theta)$, in eq 2.9, the harmonic nuclear wave function

$$\begin{aligned} \chi_0(j; R, \theta) &= \left(\frac{\alpha_R}{\pi}\right)^{1/4} H_j(\sqrt{\alpha_R/\hbar}(R - R_0)) e^{-(\alpha_R/2)(R - R_0)^2} \left(\frac{\alpha_\Theta}{\pi}\right)^{1/4} \\ &\quad \times \exp\left[-\frac{\alpha_\Theta}{2}(\theta - \theta_0)^2\right] \end{aligned} \quad (2.10)$$

where H_j is a Hermite polynomial of degree j , α_R and α_Θ are obtained from the ICN stretching and bending force constants,²⁷ and the equilibrium values of the Jacobi coordinates (R, Θ) are $R_0 = 4.99$ bohrs, and $\theta_0 = 0.0$ rad, respectively. The electronic wave function $\phi^n(\mathbf{x})$ in eq 2.9 is defined as the product of two one-dimensional harmonic oscillator wave functions, each representing the eigenfunctions of the electronic part of the quantum Hamiltonian. For example, the electronic wave function

for state n is a ground state harmonic oscillator wave function for all electronic modes except the n th one, which has one quantum of excitation:

$$\phi^n(\mathbf{x}) = x_n e^{-(1/2)(x_1^2 + x_2^2)} \quad (2.11)$$

In our calculations we use the empirical ICN potential energy surfaces derived by Goldfield et al.,²⁸ and assume that the dominant contributions to the excited state dynamics result from parallel transitions from the ground state $^1\Sigma_{0+}$ potential energy surface to the excited electronic state with $^3\Pi_{0+}$ symmetry. These empirical potentials consist of two coupled excited state potential energy surfaces, associated with the $^3\Pi_{0+}$ and $^1\Pi_1$ electronic excited states that correlate to the $I_{1/2}$ and $I_{3/2}$ channel, respectively. Rigorous comparisons with experimental data, however, might require calculations on the complete set of ab initio potential energy surfaces, e.g., those reported by Morokuma and co-workers.²⁹

III. Results

Results are presented in two sections. First, section IIIA presents the cumulative transition matrix elements obtained according to the semiclassical methodology, described in section II, and compares the results to those obtained using quantum mechanics. We considered the case where $\chi_0(j) = \chi_0(1)$ is the ground vibrational state, and $\chi_0(k) = \chi_0(3)$ is the second excited vibrational state along the R coordinate. Section IIIA also compares the semiclassical results for individual wave packet components in the E - J representation, for both the $^3\Pi_{0+}$ and the $^1\Pi_1$ electronic excited states, with the corresponding quantum mechanical results. This comparison of individual wave packet components provides a comprehensive picture of the energy dependence of individual transition matrix elements and demonstrates the ability of the semiclassical methodology to describe both real and imaginary parts of the state-to-state specific transition matrix elements associated with alternative photoexcitation pathways. Finally, section IIIB presents molecular dynamics simulation results of coherent control, after photoexcitation of an initial superposition state to various final energy levels in the \tilde{A} continuum. In particular, we provide a detailed comparison between the relative product yields obtained using semiclassical mechanics to the corresponding quantum mechanical results.

A. Transition Matrix Elements. Consider first results that correlate with the $I_{1/2}$ product channel. Besides the calculation of the photodissociation cross sections, coherent control studies require $\mu_{ij}(\xi, E)$, i.e., the off-diagonal channel-dependent complex quantities. Figure 1 compares the semiclassical (solid) and quantum (dashed) results for the modulus $|\mu_{13}(I_{1/2}, E)|$ (see panel a), and phase $\Phi_{13}(I_{1/2}, E)$ (panel b) of the cumulative transition matrix element $\mu_{13}(I_{1/2}, E)$ [see eq 2.4]. Although one sees differences of up to 15–20% between the semiclassical and quantum mechanical results, the overall qualitative features are in excellent agreement with one another; that is, both the overall shape of $|\mu_{13}(I_{1/2}, E)|$ and the position of the amplitude nodes as a function of E , as well as the energy dependence of the phase $|\Phi_{13}(I_{1/2}, E)|$ are in good agreement. Note that the phase of μ_{ij} is the most elementary phase-dependent quantity to which we can apply a test of the utility of semiclassical mechanics. That is, the phase of a matrix element involving the continuum, as opposed to the product considered herein, does not allow for quantum-semiclassical comparisons since the phase of the continuum wave function is arbitrary and therefore computer-code dependent.

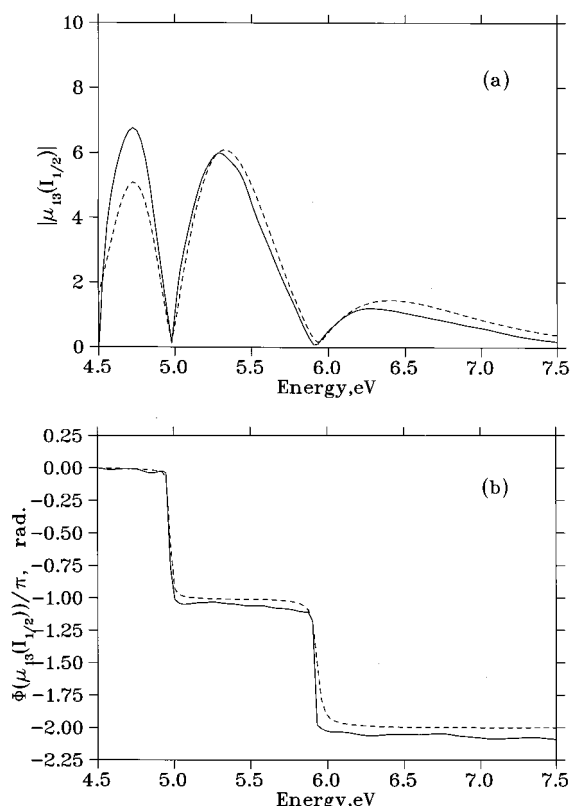


Figure 1. Semiclassical (solid lines), and quantum mechanical (dashes) cumulative matrix elements $\mu_{13}(I_{1/2}, E) = |\mu_{13}(I_{1/2}, E)| \exp(i\Phi_{13}(I_{1/2}, E))$, associated with final photodissociation channel $I_{1/2}$, as a function of final energy E in the \tilde{A} continuum.

Figure 1 shows important qualitative features of $\mu_{13}(I_{1/2}, E)$, such as the energy position of the nodes, and the change in sign of $\mu_{13}(I_{1/2}, E)$ when going through an energy node. Both of these features are determined by the symmetry properties of the product of the two wave packet components that contribute to $\mu_{13}(I_{1/2}, E)$ at each J , as defined by eq 2.4. The origin of the deviations between semiclassical and full quantum mechanical results, displayed in Figure 1, can be attributed to differences in the asymptotic wave packet components that correlate with the $I_{1/2}$ photodissociation channel, as discussed later in this section. The wave packet components also provide a comprehensive understanding of the energy dependence of $|\mu_{13}(I_{1/2}, E)|$ since, as mentioned above, $|\mu_{13}(I_{1/2}, E)|$ is obtained according to eq 2.4, by summing the product of the two wave packet components that correlate to the $I_{1/2}$ photodissociation channel over all rotational states.

Figure 2 compares contour plots for the asymptotic wave packet components that correlate to the $I_{1/2}$ photodissociation product. Results are shown for wave packet components obtained in the photoexcitation of ICN that are initially in the ground vibrational state $|\chi_0(1)\rangle$ (panel a), or in the second excited vibrational state $|\chi_0(3)\rangle$ (panel b). Here, semiclassical wave packet results (solid lines) are compared to the corresponding quantum results (dashed lines), obtained at 50 fs after photoexcitation of the molecule to the ${}^3\Pi_{0+}$ electronic excited state. At this time, the wave packet components in the E - J representation are asymptotic since the wave packet is unchanged at times greater than 45 fs after photoexcitation. Figure 2 shows that for this empirical potential energy model, the CN rotational distributions associated with both photoexcitation pathways are centered at approximately $J = 10$ for all final energy states in the \tilde{A} continuum. However, they differ with respect to one another in the number of nodes along the energy coordinate,

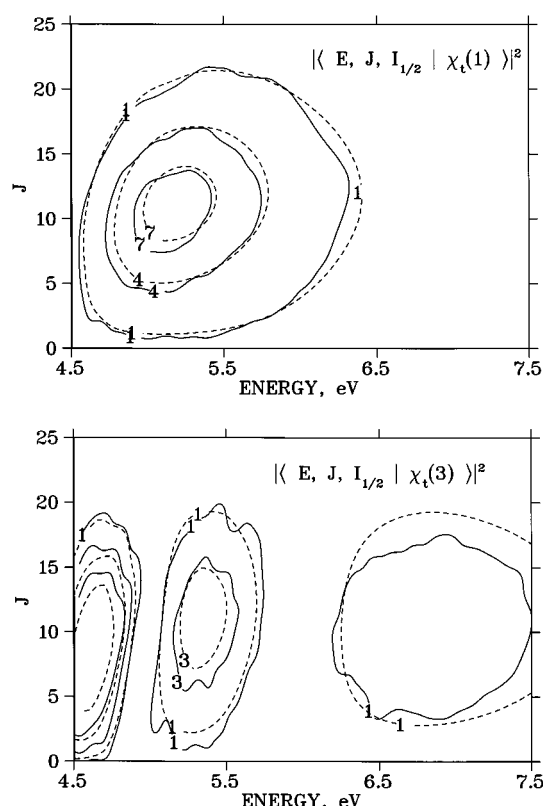


Figure 2. Contour plots for the norm of the ${}^3\Pi_{0+}$ asymptotic wave packet components in the E - J representation at 50 fs after ${}^3\Pi_{0+} \leftarrow X$ photoexcitation of the molecule that is initially in the ground (panel a), or second excited vibrational states (panel b). Semiclassical results (solid lines), and the corresponding quantum mechanical results (dashed lines) are shown.

reflecting features of the corresponding initial vibrational state. The agreement between semiclassical and full quantum mechanical calculations is quite satisfactory at the center of the band, while deviations become more significant at the tails.

Similar considerations apply to product associated with the $I_{3/2}$ channel. Figure 3 shows the modulus $|\mu_{13}(I_{3/2}, E)|$ (see panel a), and phase $\Phi_{13}(I_{3/2}, E)$ (panel b) of $\mu_{13}(I_{3/2}, E)$, and compares the semiclassical (solid lines) and quantum mechanical (dashed) results. Figure 3 shows that both the modulus and the phase of the semiclassical $\mu_{13}(I_{3/2}, E)$ are in very good agreement with quantum results. Significantly, for all cases the convergence of the modulus, and the phase, occur at essentially the same rate.

Figure 4 compares the contour plots for the asymptotic wave packet components that correlate to the $I_{3/2}$ spin-orbit state in the ${}^1\Pi_1$ photodissociation channel. These wave packets result entirely from nonadiabatic dynamics at the conical intersection, after ${}^3\Pi_{0+} \leftarrow X$ photoexcitation of ICN molecules that are initially in the ground vibrational state (panel a), or in the second excited vibrational state (panel b). As above, semiclassical wave packets (solid lines) are compared to the corresponding quantum results (dashed lines), at 50 fs. Figure 4 shows that for this photodissociation channel the CN rotational distributions associated with both photoexcitation pathways have maximum amplitudes at $40 \leq J \leq 60$ for all final energy states in the \tilde{A} continuum, and are significantly more structured than the wave packet components that correlate to the $I_{1/2}$ spin-orbit state. The agreement between semiclassical and quantum calculations, for these rather hot and complicated rotational distributions, is once again very satisfactory. Evident from Figure 4 is the origin of the two more prominent band intensities displayed by Figure 3, in the 4–6 eV energy range, as well as the quality of the

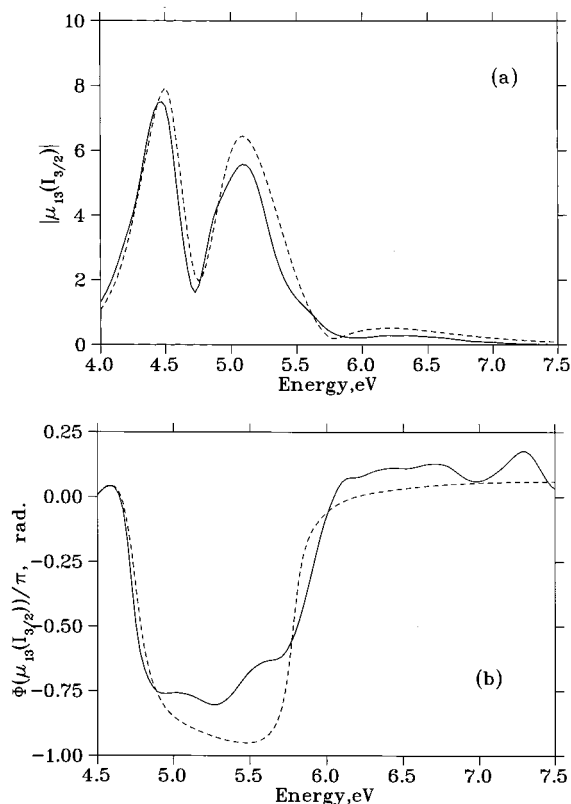


Figure 3. Semiclassical (solid lines), and quantum mechanical (dashes) cumulative matrix elements $\mu_{13}(I_{3/2}, E) = |\mu_{13}(I_{3/2}, E)|\exp(i\Phi_{13}(I_{3/2}, E))$, associated with final photodissociation channel $I_{3/2}$, as a function of final energy E in the \tilde{A} continuum.

“node” at ~ 4.75 eV as determined by the structure of the rotational distribution as a function of J . Figure 3 also shows that the same level of agreement displayed in Figure 3 for the cumulative transition matrix element as a function of energy can also be observed in the rotational state specific transition amplitudes. Thus, one would anticipate that the SC-IVR techniques could also be implemented for simulating rotational state specific CC techniques.

In these computations, we have included only contributions from parallel transitions ${}^3\Pi_{0+} \leftarrow X$, in order to facilitate the comparison between semiclassical and quantum calculations. Therefore, the cumulative transition matrix element $\mu_{13}(I_{3/2}, E)$ results exclusively from population that crosses from the initially populated ${}^3\Pi_{0+}$ state to the ${}^1\Pi_1$ electronic excited state at the conical intersection. The agreement displayed in Figure 3 demonstrates that the Meyer–Miller Hamiltonian, quantized according to the Herman–Kluk SC-IVR methodology together with stationary phase MC methods, is able to describe not only the modulus but also the phase of the off-diagonal cumulative transition matrix elements in semiquantitative agreement with full quantum mechanical calculations. This is an important result because it demonstrates that even when the system undergoes purely nonadiabatic dynamics the semiclassical methodology correctly describes both coherences, i.e., the relative phases of asymptotic wave functions in the \tilde{A} continuum, and probability distributions.

Finally, Figures 5 and 6 compare the semiclassical cumulative matrix elements $\mu_{ii}(I_{1/2}, E)$ (see panel a), and $\mu_{ii}(I_{3/2}, E)$ (see panel b), with the corresponding quantum results (dashes). With the exception of small deviations in the high energy tail of $\mu_{11}(\xi, E)$ ($\xi = {}^3/2, {}^1/2$) there is almost quantitative agreement between semiclassical and full quantum mechanical results. By contrast, Figure 6 shows somewhat poorer agreement for $\mu_{33}(I_{1/2}, E)$ (see

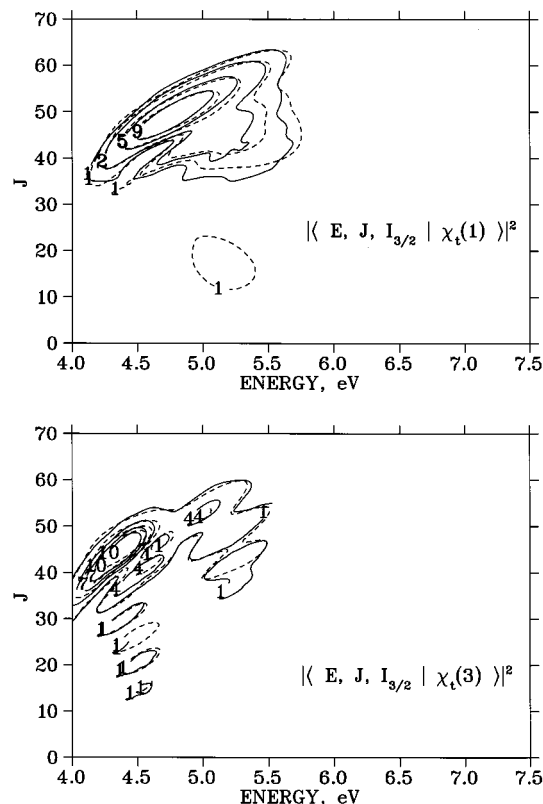


Figure 4. Comparison of contour plots for the norm of the ${}^1\Pi_1$ asymptotic wave packet components in the E – J representation at 50 fs after ${}^3\Pi_{0+} \leftarrow X$ photoexcitation of the molecule that is initially in the ground (panel a), or second excited vibrational states (panel b). Semiclassical results (solid lines), and the corresponding quantum mechanical results (dashed lines) are shown.

panel a), and $\mu_{33}(I_{3/2}, E)$ (see panel b). In this case, when the system is photoexcited from higher vibrational states, the semiclassical calculations show more significant deviations from the exact quantum mechanical results. These deviations are similar to those observed in previous studies,^{5,23,30} and are the subject of further investigation. However, the overall qualitative features of these higher vibrational state cumulative matrix elements obtained according to semiclassical mechanics are still in good agreement with full quantum mechanical calculations throughout the whole energy range.

The comparison of Figures 5, 6, 1, and 3 shows that the “nodes” of the cumulative transition matrix element are smeared out by the coupling between the two electronic states, leaving only a very narrow 5.7–6.0 eV energy range where coherent control is expected to be inefficient, since both $|\mu_{13}(I_{3/2}, E)|$ and $|\mu_{13}(I_{1/2}, E)|$ are small compared to the diagonal transition matrix elements $|\mu_{ii}(I_{3/2}, E)|$.

B. Coherent Control of Photofragmentation Product Yields. Figure 7 shows the relative product yields $R(I_{1/2}; I_{3/2}, E)$, (eq 2.3), after ICN photodissociation in the \tilde{A} continuum, obtained through bichromatic coherent control of an initial superposition of vibrational states with quantum numbers $v = 1$ and $v = 3$. Figure 7 compares the semiclassical (solid lines) and quantum (dashed lines) results obtained at various photoexcitation energies. Relative product yields are presented in the form of contour plots for the photoexcitation energies indicated in panels a–f, as a function of both the relative pulse phase parameter, $\Theta_1 - \Theta_2$, and the relative amplitude $S = c_1^2 c_1'^2 / (c_3^2 c_3'^2 + c_1^2 c_1'^2)$.

Note first, that Figure 7 shows that the product ratio varies significantly as a function of the relative pulse phase parameter,

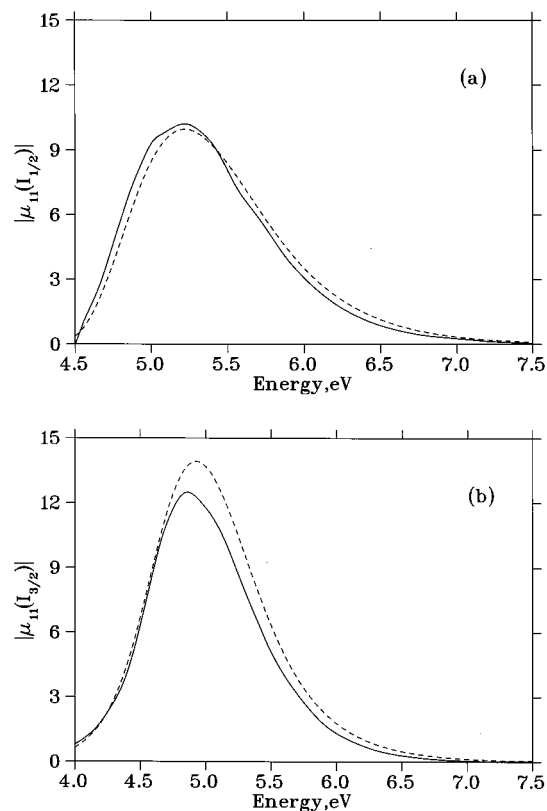


Figure 5. Semiclassical cumulative matrix elements $\mu_{11}(\xi)$, with $\xi = (I_{1/2}, I_{3/2})$ (solid lines), and the corresponding quantum mechanical results (dashes). Panel a shows the comparison of $\mu_{11}(I_{1/2})$, and panel b displays the corresponding results for $\mu_{11}(I_{3/2})$.

demonstrating a broad range of yield control over an extended range of S (i.e., strong dependence on $(\Theta_1 - \Theta_2)$) for all photoexcitation energies, with the exception of $E = 6$ eV [see panel (d)]. Here coherent control is expected to vanish since both off-diagonal matrix elements $|\mu_{13}(I_{1/2}, E)|$ and $|\mu_{13}(I_{3/2}, E)|$ are much smaller than the diagonal terms $|\mu_{ij}(\xi, E)|$, with $\xi = (I_{1/2}, I_{3/2})$ and $j = (1, 3)$ (see Figures (5, 6, 1 and 3)).

Second, note that the overall comparison between semiclassical and full quantum dynamics simulations of coherent control, displayed by the contour diagrams in Figure 7, indicates that the structure of the diagrams, the trend in these structures with photoexcitation energy, and the range of quantum mechanical product yields are reproduced by the semiclassical calculations within an error of approximately 5–10%.

At the lowest photoexcitation energy (see panel a), maximum control is attained at $S \leq 0.5$, where the production of $I_{1/2}$ can be reduced from 40% to less than 1%, simply by varying the relative phase parameter from 0° to 180° at $S \sim 0.25$. At higher values of S (as $S \rightarrow 1$), the semiclassical and full quantum mechanical product yields still agree with one another within an error of 5–10% and show a qualitatively different behavior from that observed at smaller values of S . In particular, the ratio R , as $S \rightarrow 1$, becomes only weakly dependent on the relative pulse phase parameter, $\Theta_1 - \Theta_2$, and it is therefore no longer possible to control the final outcome of the photodissociation reaction.

At higher photoexcitation energies (see panel b) the semiclassical and full quantum mechanical product yields again agree within about 5–10% error and show dependence on $\Theta_1 - \Theta_2$ and S that is completely different from that obtained at lower photoexcitation energies. Here, the degree of yield control is

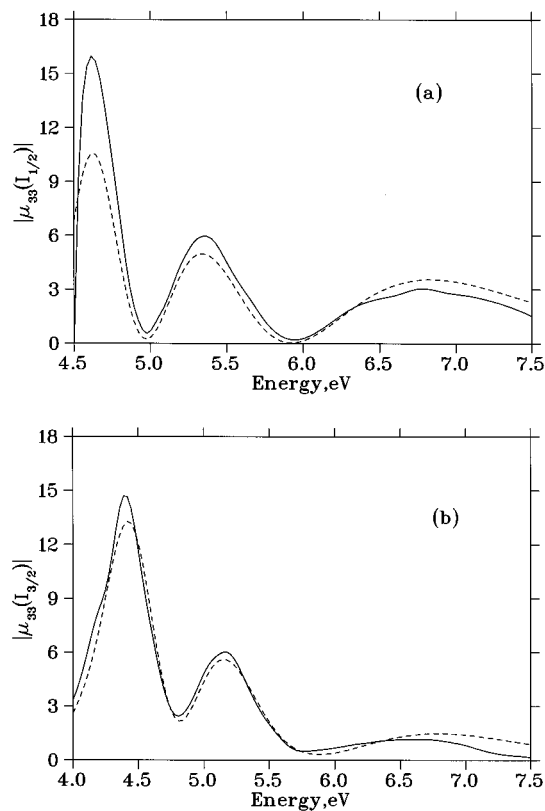


Figure 6. Semiclassical cumulative matrix elements $\mu_{33}(\xi)$, with $\xi = (I_{1/2}, I_{3/2})$ (solid lines), and the corresponding quantum mechanical results (dashes). Panel a shows the comparison of $\mu_{33}(I_{1/2})$, and panel b displays the corresponding results for $\mu_{33}(I_{3/2})$.

found to be maximum in the $0.5 \leq S \leq 0.8$ range, where the production of $I_{1/2}$ can be reduced from more than 70% to less than 30% by changing the relative phase from about 330° to 150° .

Various different trends are observed at the other energies shown in Figure 7, it being clear that (a) ICN is an excellent candidate for studies of coherent control and (b) semiclassical IVR computations do an adequate job of predicting control.

IV. Conclusions

In this article we have shown that coherent control over ICN photodissociation is extensive and that SC-IVR techniques are able to simulate bichromatic coherent control of an initial ICN superposition state in semiquantitative agreement with exact quantum mechanical results.

We have demonstrated the capabilities of a semiclassical technique that involves quantization of the Meyer–Miller classical Hamiltonian for nuclear and electronic dynamics, by comparing the semiclassical and full quantum mechanical results of relative photofragmentation product yields, as controlled by the relative pulse phase, or the relative amplitude parameters. Some quantitative disagreement was observed for dynamics initiated in the higher vibrational states. Its origin is the subject of further study.

The SC results obtained through quantization of the Meyer–Miller Hamiltonian, according to the Herman–Kluk SC-IVR methodology, together with stationary phase MC methods, were able to reproduce the correct structure of the relative product yield for various different photoexcitation energies, demonstrating that the SC-IVR methodology correctly describes excited

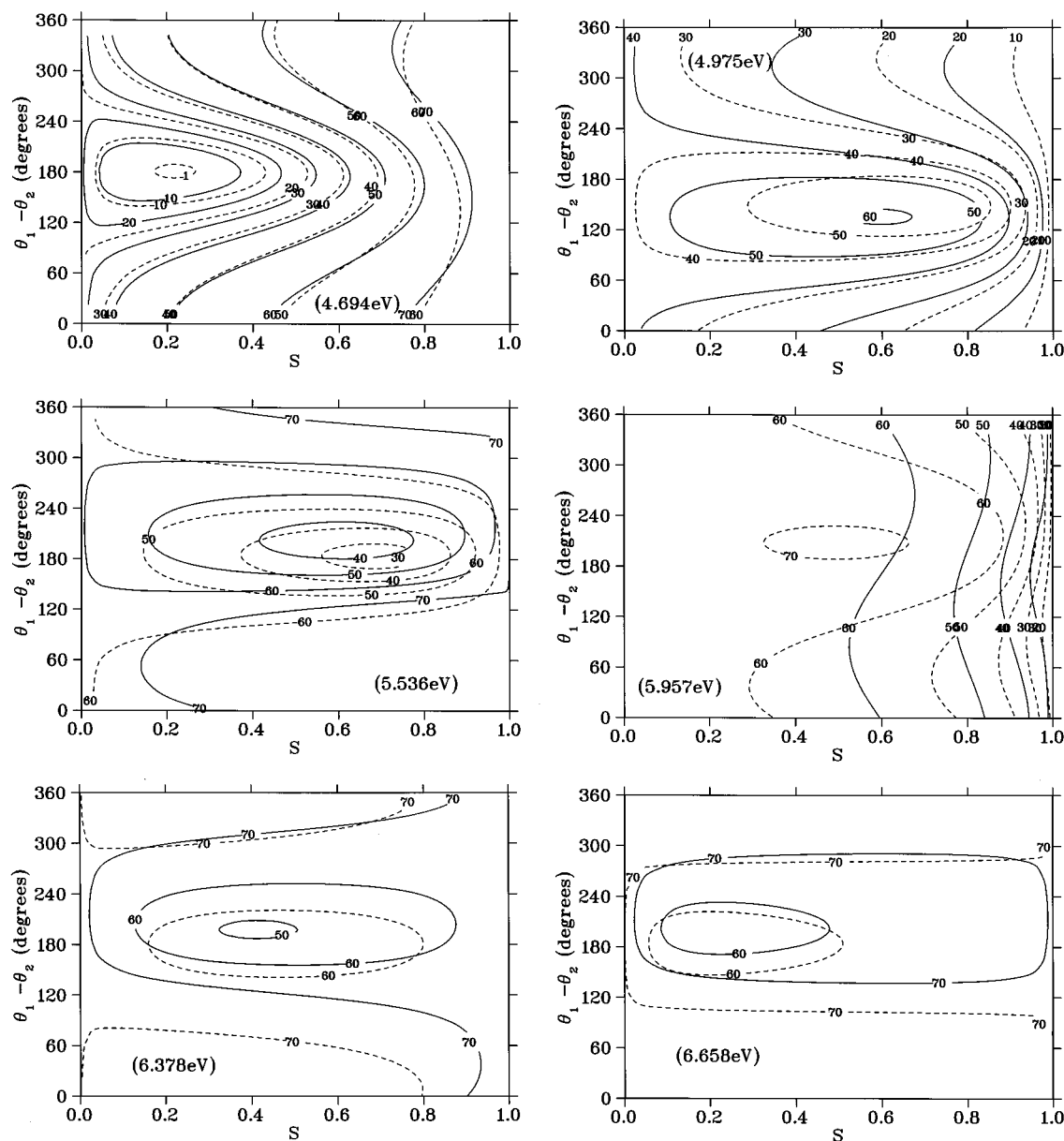


Figure 7. Contour plots of the relative product yields $R(I_{1/2}:I_{3/2}, E) = I_{1/2}/(I_{1/2} + I_{3/2})$, for bichromatic coherent control of an initial ICN superposition state with vibrational quantum numbers $\nu = 1$ and $\nu = 3$, respectively. The photoexcitation energy is indicated in each panel.

state nonadiabatic dynamics as influenced by laser induced quantum interference effects.

According to the present implementation, semiclassical simulations of ICN coherent control require the evaluation of quite a large number of trajectories ($\sim 2 \times 10^7$), and of course they would be even more demanding for systems with many more degrees of freedom. This is clearly the aspect of the calculation that needs further development. It is expected that the combination of the HK SC-IVR, together with stationary phase MC, and direct implementation methodologies under development, should provide a more tractable approach for simulating coherent control on higher dimensionality problems.

Acknowledgment. The authors are grateful to Bill Miller for teaching them many things in many different ways. We gratefully acknowledge financial support for this work from the U.S. Office of Naval Research and from Photonics Research Ontario. We also acknowledge a generous allocation of supercomputing time from the National Energy Research Scientific

Computing Center (NERSC). V.S.B. thanks Dr. Eduardo A. Coronado for very encouraging comments on an early version of this manuscript.

References and Notes

- (1) Shapiro, M.; Brumer, P. In *Advances in Atomic, Molecular and Optical Physics*; Bederson, B., Walther, H., Eds.; Academic Press: San Diego, CA, 2000; pp 287–343.
- (2) Brumer, P.; Shapiro, M. *Chem. Phys. Lett.* **1996**, 126, 541.
- (3) Shapiro, M.; Brumer, P. *Faraday Discuss. Chem. Soc.* **1987**, 82, 177.
- (4) Miller, W. H. *J. Chem. Phys.* **1970**, 53, 3578.
- (5) Batista, V. S.; Miller, W. H. *J. Chem. Phys.* **1998**, 108, 498.
- (6) Batista, V., et al., *J. Chem. Phys.* **1999**, 110, 3736.
- (7) Guallar, V.; Batista, V.; Miller, W. H. *J. Chem. Phys.* **1999**, 110, 9922.
- (8) Campolieti, G.; Brumer, P. *Phys. Rev. A* **1994**, 50, 997.
- (9) Kay, K. G. *J. Chem. Phys.* **1994**, 100, 4432.
- (10) Kay, K. G. *J. Chem. Phys.* **1994**, 101, 2250.
- (11) Brewer, M. L.; Hulme, J. S.; Manolopoulos, D. E. *J. Chem. Phys.* **1997**, 106, 4832.

- (12) Guerin, B. E.; Herman, M. F. *Chem. Phys. Lett.* **1998**, 286, 361.
- (13) Heller, E. J. *Chem. Phys.* **1991**, 95, 9431.
- (14) Grossmann, F.; Heller, E. J. *Chem. Phys. Lett.* **1995**, 241, 45.
- (15) Garashchuk, S.; Grossmann, F.; Tannor, D. J. *J. Chem. Soc., Faraday Trans.* **1997**, 93, 781.
- (16) Shalashilin, D. V.; Jackson, B. *Chem. Phys. Lett.* **1998**, 291, 143.
- (17) Provost, D.; Brumer, P. *Phys. Rev. Lett.* **1995**, 74, 250.
- (18) Guo, H.; Schatz, G. C. *J. Chem. Phys.* **1990**, 92, 1634.
- (19) Meyer, H.; Miller, W. H. *J. Chem. Phys.* **1979**, 70, 3214.
- (20) Tully, J. *J. Chem. Phys.* **1990**, 93, 1061.
- (21) Stock, G.; Thoss, M. *Phys. Rev. Lett.* **1997**, 78, 578.
- (22) Wang, H.; Song, X.; Chandler, D.; Miller, W. *J. Chem. Phys.* **1999**, 110, 4828.
- (23) Coronado, E. A.; Batista, V. S.; Miller, W. H. *J. Chem. Phys.* **2000**, 112, 5566.
- (24) H. W. P.; L. S. R., *J. Chem. Phys.* **1987**, 86, 3773.
- (25) Nadler, I.; Mahgerefteh, D.; Reisler, H.; Wittig, C. *J. Chem. Phys.* **1985**, 82, 3885.
- (26) Pitts, W.; Baronavski, A. *Chem. Phys. Lett.* **1980**, 71, 395.
- (27) Herzberg, G. *Molecular Spectra and Molecular Structure, Volume II*; Krieger Publishing Co: Malabar, FL, 1991; p 174.
- (28) Goldfield, E. M.; Houston, P. L.; Ezra, G. S. *J. Chem. Phys.* **1986**, 84, 3120.
- (29) Qian, J.; Tannor, D.; Amatatsu, Y.; Morokuma, K. *J. Chem. Phys.* **1994**, 101, 9597.
- (30) Sun, X.; Miller, W. H. *J. Chem. Phys.* **1999**, 110, 6635.